Small-Signal Stability Analysis of Type-4 Wind in Series Compensated Networks

Yangkun Xu, *Student Member, IEEE*, Miao Zhang, *Student Member, IEEE*, Lingling Fan, *Senior Member, IEEE*, Zhixin Miao, *Senior Member, IEEE*

***Abstract*—Type-4 wind is claimed to be immune from subsynchronous resonances (SSRs) that have been experienced by Type-3 wind with radial connection to series compensated lines. In this paper, we examine this claim through simplified analytical model building, analysis based on linearized models, and validation against electromagnetic transient (EMT) testbeds with full details. Two analytical models of Type-4 wind farm with radial connection to a series compensated line are built in dq-frames. The main difference of the two models is in grid-side converter (GSC)'s control mode, with one model assuming real power control and the other assuming dc-link voltage control. Relying on the analytical models, an efficient approach is demonstrated to obtain frequency-domain impedance models. Small-signal analysis is carried out using eigenvalue analysis and frequency-domain impedance model-based analysis. Potential stability risk is demonstrated, which is due to interaction of a mode associated to voltage source converter (VSC) in weak grid (termed as "weak grid mode") and a mode associated to network LC resonance. The weak grid mode is influenced by grid strength and VSC control parameters, including phase-locked-loop (PLL) parameters. The small-signal analysis results are validated against two EMT testbeds with full details in MATLAB/SimPowerSystems and PSCAD/EMTDC, respectively.**

***Index Terms*—Type-4 wind farm; subsynchronous resonances (SSR); series compensation; phase-locked-loop (PLL)**

I. Introduction

SINCE 2009, SSR events due to Type-3 wind radial connection with series compensated transmission lines have been observed in Texas [1], [2] and North China [3]. In 2017, three SSR events occurred in South Texas [2].

It is natural to pose this question: Are type-4 wind farms immune to SSRs? Very few research exists to address this question except [4] and [5]. PSCAD simulation studies in [4] demonstrate that a type-4 wind with its grid side converter (GSC) in active power and ac voltage control mode is immune from SSR issues. This remark is also stated in [3], where the authors remarked that based on observations from real-world SSR events, type-4 wind made no contribution to SSR.

Strong grid assumption is made in the study systems in [3], [4]. On the other hand, real-world stability issues due to voltage-source converter (VSC) with weak grid interconnection have manifested as 4 Hz oscillations in Texas wind farms [6] and 30 Hz oscillations in west China type-4 wind farms [7]. Research has been carried out on VSC in weak grids, e.g., [8]–[16].

Y. Xu, M. Zhang, L. Fan and Z. Miao are with Dept. of Electrical Engineering, University of South Florida, Tampa FL 33620. Emails: linglingfan@usf.edu.

It is thus natural to examine stability issues of type-4 wind farms in series compensated networks while considering weak grid condition. The only existing research that conducts small-signal stability analysis of type-4 wind farm in series compensated grids with weak grid consideration is [5]. Reference [5] uses analytical modeling approach (impedance-based approach) to study this engineering problem. Type-4 wind turbine's grid side converter (GSC) is assumed in dc-link voltage control mode. The findings of [5] indicate that there are potential stability risks due to non-passivity of type-4 wind admittance in subsynchronous frequency range. GSC control (e.g., PLL parameters, reactive power control), and GSC operating condition (e.g., active power exporting level) influences the non-passivity.

While [5] identified potential stability risks due to non-passivity of GSC, non-passivity cannot be used to explain the particular dynamics that may be associated with series compensated network. In addition, the stability analysis method presented in [5] does not offer a whole picture of the entire system's dynamic modes. Validation against electromagnetic transient (EMT) testbeds with full details is also missing.

This paper aims to conduct a thorough analysis with validation and offer insights. Through state-space model building and eigenvalue based analysis, quantitative measure and physical insights will be offered in this paper. The major engineering discovery from this research is that the interaction of a mode associated with GSC in weak grid (termed as "weak grid mode") and a mode associated with network LC resonance may lead to instability. The weak grid mode moves to the left half plan (LHP) when grid strength is increased for noncompensated network. However, due to LC mode interaction, it moves to the right half plane (RHP) when series compensation increases to improve grid strength.

Type-4 wind's GSC either assumes dc-link voltage control or active power control [17] (Chapter 9). Large size type-4 wind farms's GSCs prefers power control mode [18]. This fact is also confirmed by [4], a study carried out by Siemens where power control mode is assumed for GSC. Hence, in this paper, two types of type-4 wind farms investigated: GSC in power control mode and dc-link voltage control mode.

This paper also aims to provide a powerful modeling framework to carry out small-signal analysis. For inverter-based resource (IBR) grid integration dynamic studies, there are two major analytical model building approaches: state-space based time-domain modeling approach (e.g., [19]) and impedance-based frequency domain modeling approach (e.g., [20]–[23]). Impedance model-based method relies on derivation of linear models that represent voltage and current relationship block by block, assembling of impedances, and Nyquist stability criterion-based analysis. Reference [5] falls into the second category where the wind turbine impedance model is derived through a manual process.

With state-space analytical models, frequency-domain impedance models can be efficiently derived. Both eigenvalue analysis and impedance model-based stability analysis are carried out in this research.

Study approach wise, an efficient impedance derivation method relying on nonlinear large-signal analytical models is presented. Both eigenvalue analysis and frequency-domain impedance-based stability analysis are conducted. This paper thus demonstrates the power of state-space modeling approach.

Our contribution and novelty lie in four aspects:

- a comprehensive scope of work that investigates two major types of type-4 wind turbines for grid integration into series compensated networks;
- a rigorous study approach that has analytical results based on simplified models validated by simulation results based on EMT models with full details;
- a powerful modeling frame with the capability of not only well-known eigenvalue analysis, participation factor analysis but also impedance-based frequency-domain stability analysis;
- an insightful finding of potential stability issues in series compensated grids with high penetration of type-4 wind.

The rest of the paper is structured as follows. Section II gives a brief introduction of the type-4 wind grid integration testbeds and the two corresponding analytical models. Section III and IV present small-signal analysis analysis and EMT validation for the two systems, respectively. Section V presents impedance model derivation and stability analysis. Finally, the conclusions are drawn in Section VI.

II. Type-4 wind testbeds and Analytical Models

A. Testbeds

The outer control of a type-4 wind turbine's GSC may assume dc-link voltage control mode or real power control mode. Thus, two testbeds reflecting this difference are adopted in this paper for validation.

The first testbed is a 5 MW type-4 wind grid integration system in PSCAD/EMTDC. The schematic diagram of Testbed 1 is shown in Fig. 1a. This type-4 wind turbine consists of a permanent magnet synchronous generator (PMSG) to convert mechanical energy to electric energy, and a back-to-back voltage source converters to convert variable frequency ac to 60 Hz ac. This testbed is developed from a demo system in PSCAD/EMTDC where the machine-side converter (MSC) realizes Maximum Power Point Tracking (MPPT) and the GSC assumes dc-link voltage control. The testbed is adjusted to have the GSC realize MPPT control so the outer control of GSC is in real power control mode. The MSC is adjusted to control dc-link voltage. Between the two converters, there is a dc chopper employed to avoid overvoltage on the dc-link capacitor [24].

The second testbed is developed based on a demo system in MATLAB/SimPowerSystems. Fig. 1b shows the 100 MW type-4 wind grid integration testbed with GSC in dc-link voltage control mode. The electricity generated by a synchronous generator is rectified to dc electricity through a diode-bridge rectifier. The dc electricity then passes through a dc/dc boost converter to achieve dc voltage at a different voltage level. MPPT is implemented in the dc/dc boost converter. The parameters of the system are shown in Table V in Appendix.

B. Analytical Models

Two analytical models are built to reflect the two testbeds. In analytical models, wind turbine representation is simplified with only GSC control included. For GSC with dc-link voltage control mode, the dc-link capacitor dynamics is also included. These two models are adapted from the models developed in [14], [15] for wind in weak grid research. For this study, the grid dynamics now include LC resonance dynamics.

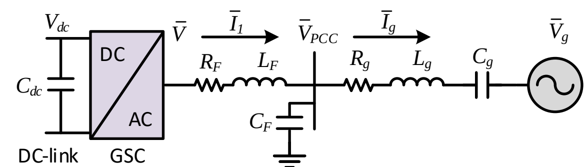

Fig. 2: A type-4 wind farm with radial connection to a series compensated line .

Fig. 2 presents the system circuit topology. The analytical models are presented in Fig. 3, to represent the study system. The analytical models are based on dq-frames. Hence, at steady-state, all state variables are constant. With this feature, linear models can be derived using numerical perturbation.

In Model 1, GSC is in power control mode. The power order is assumed to be a known parameter. In Model 2, GSC is in dc-link voltage control mode.

1) GSC control: GSC's inner current control and outer control all adopt proportional-integral (PI) controllers and are modeled in the converter dq-reference frame, notated by superscript 'c'. The converter frame is based on the PLL output angle. The angle of the PCC voltage is estimated by the PLL. At steady-state, the PLL output angle is the same as the PCC voltage angle which results in the converter frame d-axis aligning with the PCC voltage space vector. At transient conditions, the PCC voltage angle and PLL output angle have difference.

The GSC converter voltage (v_d^c, v_q^c) are generated from the current control with PCC voltage feedforward and cross coupling items considered. The current orders are determined by the outer power/dc-link voltage control and ac voltage control, respectively. Modeling details related to VSC grid integration can be referred from [14].

2) PLL: Effect of PLL parameters on stability is examined. A simple second-order PLL is assumed. Structure of the PLL can be found in [14]. Two sets of parameters are considered. PLL 1 has proportional and integral gains as (60, 1400). PLL 2 has proportional and integral gains as (150, 10000). The two PLLs have bandwidths of 13 Hz and 32 Hz respectively. Their

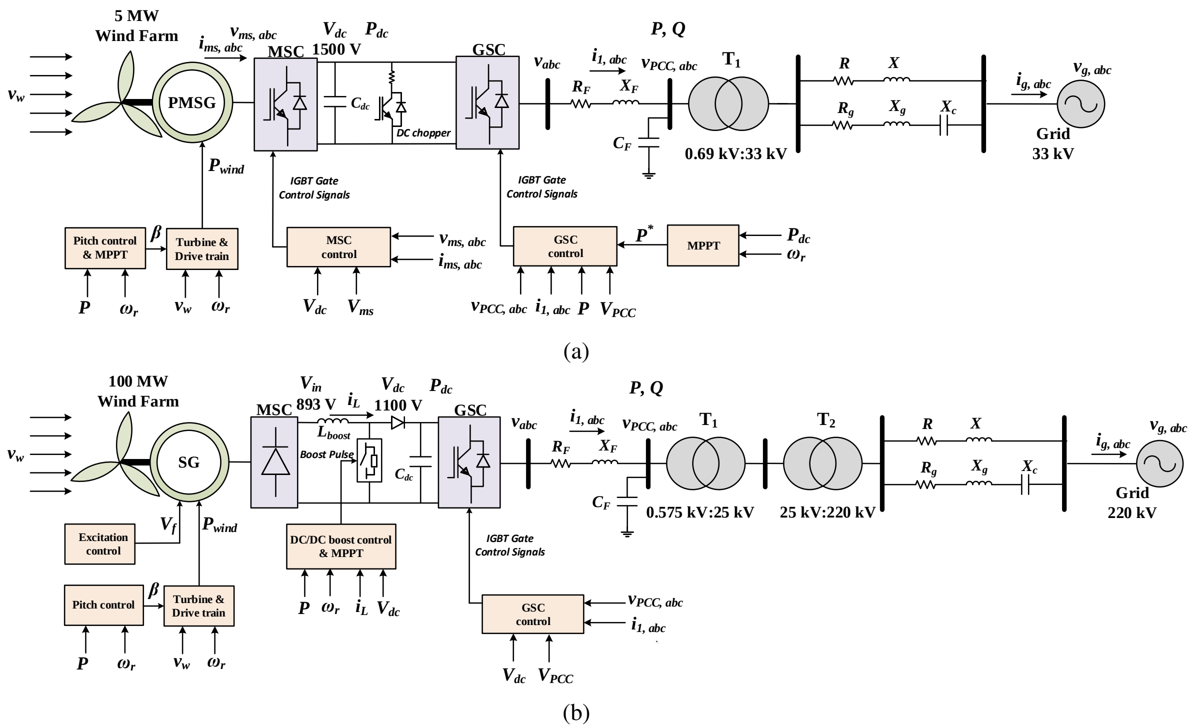

Fig. 1: EMT testbeds of type-4 wind in series compensated networks. (1a) P control implemented in PSCAD/EMTDC testbed. (1b) V_{dc} control implemented in MATLAB/SimPowerSystems testbed.

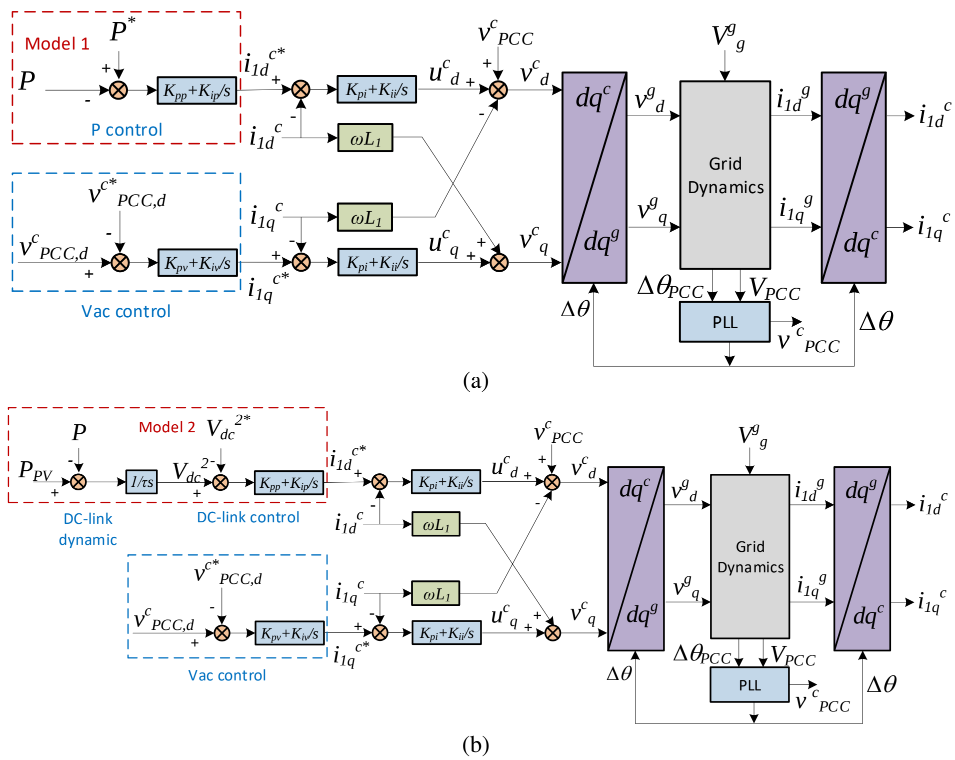

Fig. 3: Analytical models. (3a) Model 1 with GSC in power control mode and (3b) Model 2 with GSC in dc-link voltage control mode.

close-loop transfer functions from the input angle to the output angle are plotted and shown in Fig. 4.

3) Grid dynamics: The grid dynamics are modeled in the grid dq-reference frame, which rotates at the nominal speed ω_0. This frame is denoted by superscript 'g'.

The grid dynamics block has the converter voltage and grid voltage as input or known parameters. Both the converter voltage and the grid voltage are assumed to be three-phase balanced. At stead-state, their dq-frame variables all assume constant values.

The state variables of the grid dynamics block include the series capacitor voltage, the shunt capacitor voltage, the grid current and the converter output current, all in dq-frame. Total, there are eight state variables.

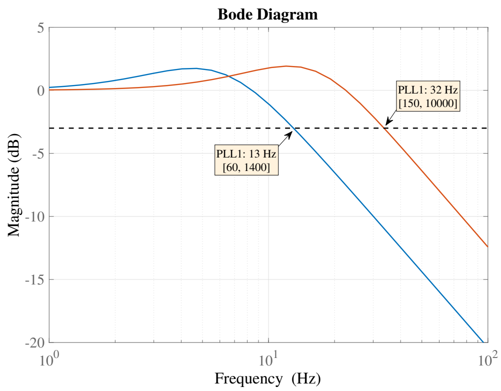

Fig. 4: PLL with different bandwidth: PLL 1: (60, 1400) with bandwidth as 13 Hz. PLL 2: (150, 10000) with bandwidth as 32 Hz.

The grid dynamics in the grid dq-frame can be derived from abc-frame space vector based differential equations. The dq-frame differential equations are expressed as follows:

$$
\begin{cases}
\frac{di_{1d}^g}{dt} &= \frac{1}{L_F}(v_d^g - v_{PCC,d}^g - R_F i_{1d}^g + L_F\omega_0 i_{1q}^g) \\
\frac{di_{1q}^g}{dt} &= \frac{1}{L_F}(v_q^g - v_{PCC,q}^g - R_F i_{1q}^g - L_F\omega_0 i_{1d}^g) \\
\frac{di_{g,d}^g}{dt} &= \frac{1}{L_g}(v_{PCC,d}^g - v_{c,d}^g - v_{g,d}^g - R_g i_{g,d}^g + L_g\omega_0 i_{g,q}^g) \\
\frac{di_{g,q}^g}{dt} &= \frac{1}{L_g}(v_{PCC,q}^g - v_{c,q}^g - v_{g,q}^g - R_g i_{g,q}^g - L_g\omega_0 i_{g,d}^g) \\
\frac{dv_{PCC,d}^g}{dt} &= \frac{1}{C_F}(i_{1d}^g - i_{g,d}^g + C_F\omega_0 v_{PCC,q}^g) \\
\frac{dv_{PCC,q}^g}{dt} &= \frac{1}{C_F}(i_{1q}^g - i_{g,q}^g - C_F\omega_0 v_{PCC,d}^g) \\
\frac{dv_{c,d}^g}{dt} &= \frac{1}{C_g}(i_{g,d}^g + C_g\omega_0 v_{c,q}^g) \\
\frac{dv_{c,q}^g}{dt} &= \frac{1}{C_g}(i_{g,q}^g - C_g\omega_0 v_{c,d}^g)
\end{cases}
$$

where i_{1d}^g, i_{1q}^g, $i_{g,d}^g$, $i_{g,q}^g$, v_d^g, v_q^g, $v_{PCC,d}^g$, $v_{PCC,q}^g$, $v_{c,d}^g$, $v_{c,q}^g$ and $v_{g,d}^g$, $v_{g,q}^g$ are the d and q components of the converter current, grid current, converter voltage, PCC voltage, capacitor voltage, and grid voltage.

III. Model 1 Analysis and Validation

The analytical model (Model 1) with GSC in active power control model is shown in Fig. 3a. The system is assumed to operate and send out 1 pu wind power to grid ($P = 1$) and the PCC voltage is at nominal level ($V_{\text{PCC}} = 1$ pu). The grid strength without series compensation is assumed to be weak ($X_g = 1$ pu). The analytical model is linearized under various operation conditions to obtain linear models and small-signal analysis are followed. Validation is carried out using the PSCAD/EMTDC testbed with full dynamics.

A. Eigenvalues and Participation Factor Analysis

The series compensation (sc) level varies from 10% to 75% with a step size of 2.5%. The eigenvalues are plotted and presented in Fig. 5. Figs. 5a and 5b demonstrate the effect of PLL on system stability. Fig. 5c and Fig. 5d are the zoom in plots focusing on the subsynchronous range.

Three modes of less than 100 Hz frequencies are identified to be influenced significantly by series compensation.

It is found that when PLL has a low bandwidth, the dominant mode is a 3 Hz mode. With series compensation increasing, this mode moves to the left-half-plane (LHP) and the system becomes more stable. On the other hand, when PLL has a higher bandwith, the dominant mode is a 15 Hz mode. With series compensation increasing, this mode moves to the right-half-plane (RHP) and the system becomes less stable. If series compensation is at 27.5% or more, the system loses stability.

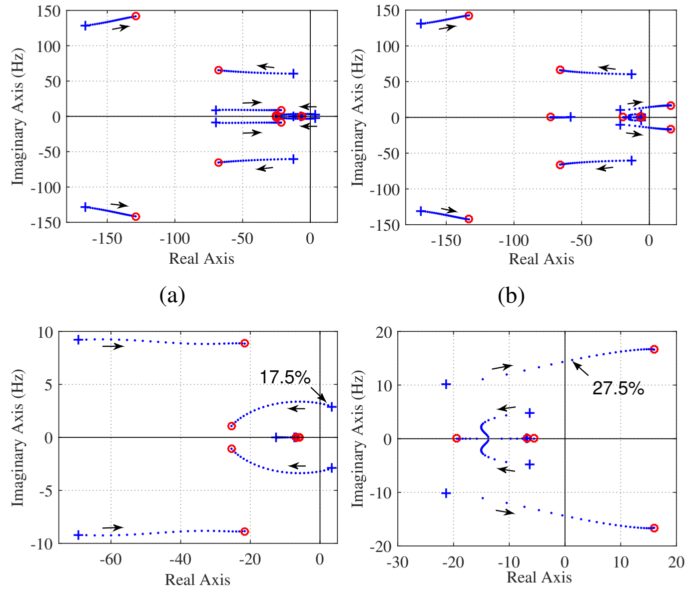

(a) (b)

(c) (d)

Fig. 5: Eigenvalues loci for Model 1 where GSC is in power control mode. (5a) adopt PLL 1. (5b) adopt PLL 2. (5c)(5d) are zoom in plots of (5a)(5b) focusing on the subsynchronous range.

TABLE II: PFs of modes $\lambda_{6,7}$, $\lambda_{8,9}$ and $\lambda_{10,11}$ in Model 1

Description	State Variable	Power control					
		PLL1(sc=17.5%)			PLL2(sc=27.5%)		
		$\lambda_{6,7}$	$\lambda_{8,9}$	$\boldsymbol{\lambda_{11,12}}$	$\lambda_{6,7}$	$\boldsymbol{\lambda_{8,9}}$	$\lambda_{11,12}$
Grid	$i_{1,d}^g$	0.0090	0.0738	0.0012	0.0168	0.0210	0.0083
	$i_{1,q}^g$	0.0082	0.0654	0.0120	0.0107	0.0563	0.0200
	$i_{g,d}^g$	0.0172	**0.4029**	0.0338	0.0233	**0.2042**	0.0588
	$i_{g,q}^g$	0.0060	**0.2577**	0.0289	0.0180	**0.2630**	0.0123
	$v_{PCC,d}^g$	0.0270	0.0492	0.0046	0.0615	0.0436	0.0014
	$v_{PCC,q}^g$	0.0544	0.0775	0.0046	0.0662	0.0373	0.0080
	$v_{c,d}^g$	**0.4642**	0.0496	0.0050	**0.4209**	0.0869	0.0048
	$v_{c,q}^g$	**0.4400**	0.0741	0.0066	**0.4163**	0.0698	0.0173
PLL	$\Delta\theta$	0.0011	**0.3879**	**0.3823**	0.0032	**0.6262**	0.1143
	$\Delta\omega$	0.0001	**0.1293**	**0.2891**	0.0006	**0.3644**	0.1417
Outer-loop	i_{1d}^c	0.0114	**0.5198**	**0.3279**	0.0178	0.1600	**0.6892**
	i_{1q}^c	0.0013	0.089	**0.4367**	0.0014	0.1045	**0.5567**
Inner-loop	u_d	0.0002	0.0023	0.0020	0.0004	0.0012	0.0040
	u_q	0.0001	0.0259	0.0718	0.0001	0.0280	0.0348

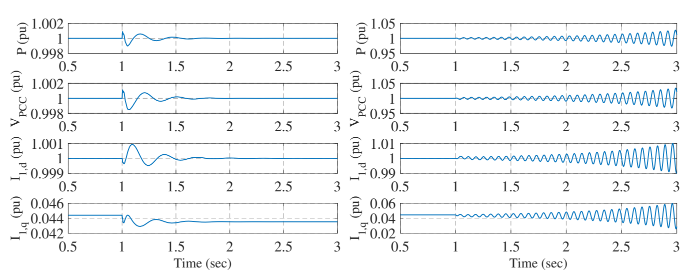

(a) (b)

Fig. 6: Model 1 dynamic response following an event of a line trip at 1 sec. sc=27.5% with power control mode. (6a): PLL 1. (6b): PLL 2.

The eigenvalues at two marginal sc conditions are presented in Table I. There are fourteen eigenvalues in Model 1. Participation factors (PFs) are computed for each eigenvalue to

TABLE I: Modes description for the power control under marginal conditions

	Modes	Eigenvalue	Damping ratio	Freq. (Hz)	Most relevant states
PLL 1 (sc=17.5%)	$\lambda_{1,2}$	$-532.6 \pm 1856.0i$	0.276	295.4	C_F, L_g
	λ_3	-1260.7	-	-	-
	$\lambda_{4,5}$	$-160.8 \pm 816.2i$	0.193	129.9	C_F, L_g
	$\lambda_{6,7}$	$-21.2 \pm 381.3i$	0.056	60.7	C_g
	$\lambda_{8,9}$	$-62.3 \pm 58.1i$	0.731	9.3	PLL, Outer loop PI, L_g
	λ_{10}	-12.6	-	-	-
	$\boldsymbol{\lambda_{11,12}}$	$\mathbf{0.1 \pm 20.1}\boldsymbol{i}$	**0.005**	**3.2**	**PLL, Outer loop PI**
	λ_{13}	-6.9	-	-	-
	λ_{14}	-7.3	-	-	-
PLL 2 (sc=27.5%)	$\lambda_{1,2}$	$-592.2 \pm 1866.7i$	0.302	297.1	C_F, L_g
	λ_3	-1259	-	-	-
	$\lambda_{4,5}$	$-157.5 \pm 842.1i$	0.184	134.0	C_F, L_g
	$\lambda_{6,7}$	$-32.5 \pm 385.0i$	0.084	61.3	C_g
	$\boldsymbol{\lambda_{8,9}}$	$\mathbf{1.3 \pm 92.2}\boldsymbol{i}$	**0.014**	**14.7**	**PLL,** $\boldsymbol{L_g}$
	λ_{10}	-66.5	-	-	-
	$\lambda_{11,12}$	$-15 \pm 14.9i$	0.709	2.4	Outer loop PI
	λ_{13}	-6.9	-	-	-
	λ_{14}	-6.9	-	-	-

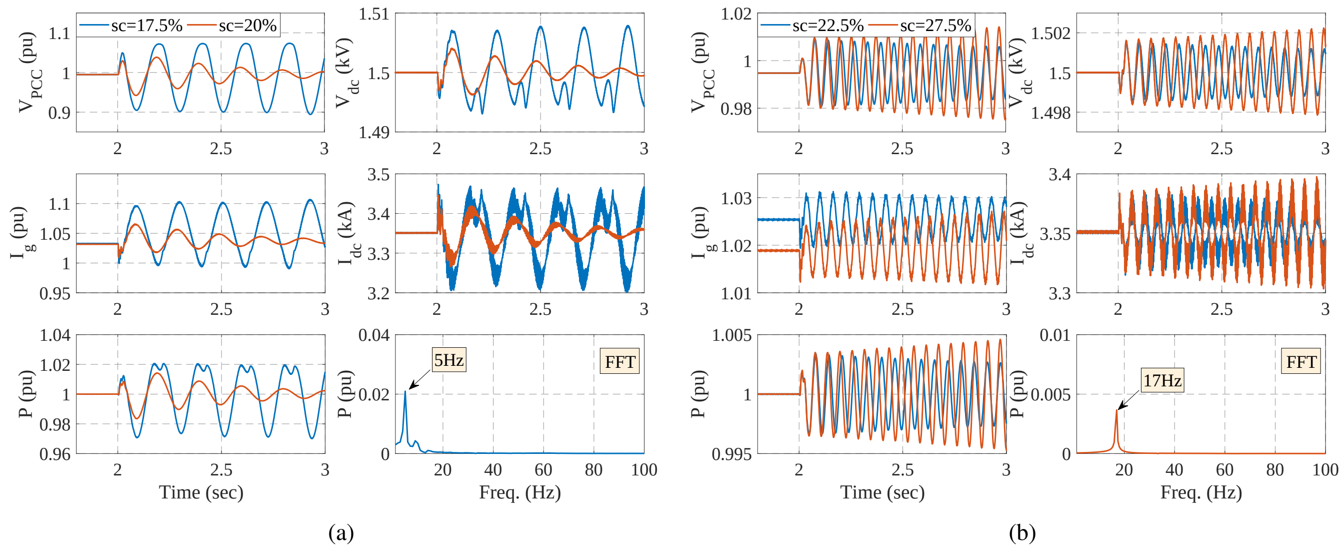

Fig. 8: Dynamic performances of two compensation level under P control in PSCAD/EMTDC. (8a) PLL 1. (8b) PLL 2.

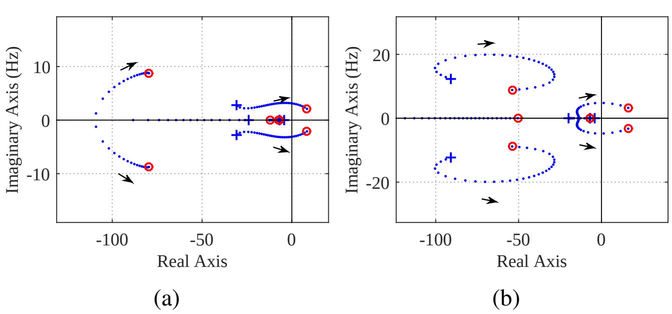

Fig. 7: Model 1 eigenvalue loci for reduced grid strength for non-compensated transmission line. (7a) PLL 1. (7b) PLL 2.

identify the most influential states. The info has been listed in Table I. Unstable modes are highlighted in bold fonts. It can be seen that there are two modes $\lambda_{1,2}$, $\lambda_{4,5}$ above 100 Hz located in the left half-plane (LHP) far from the imaginary axis. PF analysis indicates that the two modes are related to shunt capacitor and transmission line inductance.

The PFs are computed for the three modes under 100 Hz: mode $\lambda_{6,7}$ in the range of $60 \sim 65$ Hz, mode $\lambda_{8,9}$ in the range of $8 \sim 20$ Hz, and a mode $\lambda_{11,12}$ of about $3 \sim 5$ Hz, are listed in Table II.

Table II indicates that $\lambda_{6,7}$ and $\lambda_{8,9}$ are related to the series RLC circuit dynamics. The $60 \sim 65$ Hz mode $\lambda_{6,7}$ moves to the LHP with an increasing series compensation level, while the $8 \sim 20$ Hz mode $\lambda_{8,9}$ moves to the RHP.

In the subsynchronous frequency range, the two oscillation modes $\lambda_{11,12}$ and $\lambda_{8,9}$ are affected significantly by the compensation level and PLL. The lower frequency mode $\lambda_{11,12}$ tends to move to left, while the higher frequency mode $\lambda_{8,9}$ tends to move to right. For the slower PLL with a lower bandwidth (PLL 1), the low-frequency mode at 3 Hz is the dominant mode and this mode moves to LHP with an increasing sc. Hence, increasing sc poses no risk of stability.

For the faster PLL with a higher bandwidth (PLL 2), the $8 \sim 20$ Hz frequency mode poses potential stability issues. When sc increases, this mode moves towards RHP. Higher PLL bandwidth makes this mode move further to the RHP.

Time-domain simulation results using Model 1 are presented in Fig. 6. The system initially operates with parallel transmission lines (one RL circuit and one RLC circuit). 27.5 % compensation level is assued. At $t = 1$ s, the RL circuit trips. For PLL 1, the system is stable. For PLL 2, the system is unstable. The results corroborate with the eigenvalue analysis.

B. Weak Grid Modes in Non-compensated grid

As a comparison, we present eigenvalue loci in Fig. 7 when there is no series compensation. X_g is varying from 0.2 pu to 1 pu with a step size of 2.5% to reflect a reducing grid strength. It can be seen the two modes in the frequency range of 2 $\sim$ 20 Hz move to right with the grid strength reducing. These two modes can be classified as modes related to weak grids. Increasing compensation level is similar as strengthening the grid. Thus, it is reasonable that the low frequency mode of 2-5 Hz moves to the left for an increasing compensation level. On the other hand, due to the interaction of the RLC mode at about 60 Hz, the mode in range of 8 $\sim$ 20 Hz will move to the right for an increasing compensation level.

C. EMT Testbed Validation

Finally, EMT testbed validation is given. In Testbed 1 shown in Fig. 1a, a type-4 based wind farm is connected to the power grid through two parallel power lines (one non-compensated line and one series compensated line). The non-compensated line is tripped due to a fault. Subsequently, the wind farm become radially connected to the series compensated line.

The dynamics of the PCC voltage, transmission line current, real power export from the wind, dc-link voltage, dc side current and Fast Fourier transform (FFT) of wind power export P are shown in Fig. 8. At $t = 2$ s, the RL circuit is tripped. The system suffers a 5 Hz oscillations if PLL 1 is applied. Increasing the compensation level leads to enhanced stability. On the other hand, the system will suffer 17 Hz oscillations with PLL 2 in place. Moreover, these oscillations will be more severe if the series compensation increases.

The performance aligns with the analytical results presented in Fig. 5. If PLL 1 is applied, with the increasing compensation level, the low frequency mode will move to the LHP and the system is more stable. If PLL 2 is applied, the 8 $\sim$ 20 Hz mode becomes the dominant mode. Increasing series compensation level may cause instability.

IV. Model 2 Analysis and Validation

In Model 2, GSC adopts dc-link voltage control mode, as shown in Fig. 3b. The system is assumed to operate at $V_{dc} = 1$ pu, $V_{PCC} = 1$ pu and $X_g = 0.7$ pu. Testbed 2 in MATLAB/SimPowerSystems will be used for validation. The system parameters are given in the Table V in Appendix.

A. Eigenvalues and Participation Factor Analysis

Fig. 9 presents the eigenvalue loci with the series compensation level (sc) varying from 10% to 75% with a step size of 2.5%. Figs. 9c and 9d are the zoom-in plots of Figs. 9a and 9b for subsynchronous range modes. There are fifteen states and fifteen eigenvalues in Model 2. They are listed in Table III along with the influential states. Further, Table IV presents participation factors for the three modes with frequency below 100 Hz.

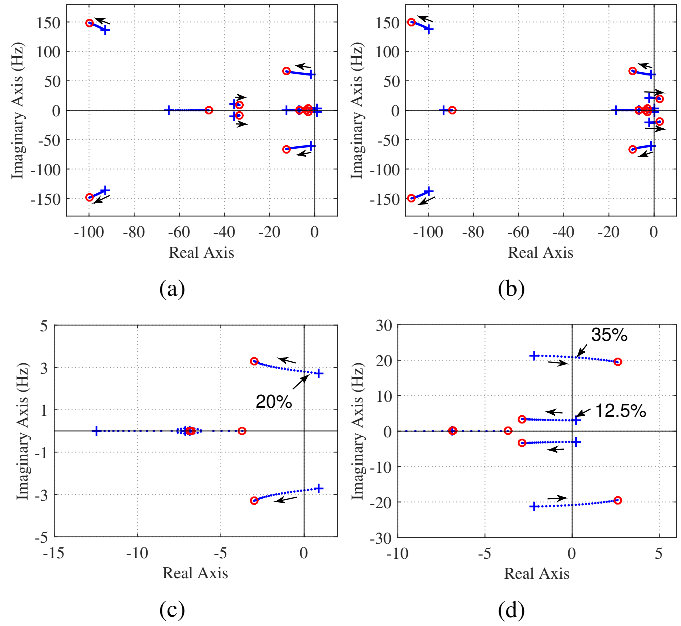

Fig. 9: Eigenvalues loci for Model 2 where GSC is in V_{dc} control mode. (9a) adopt PLL 1. (9b) adopt PLL 2. (9c)(9d) are zoom in plots of (9a)(9b) focusing on the subsynchronous range.

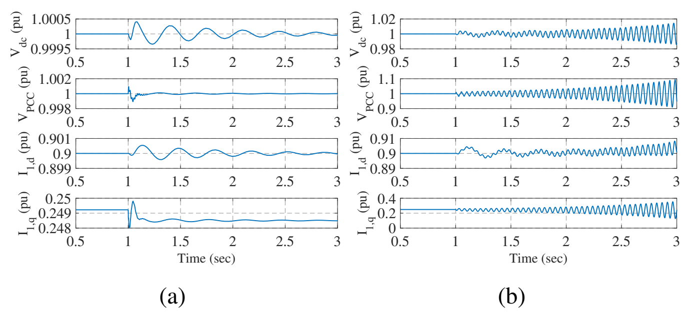

Fig. 10: Model 2 dynamic responses following an event of a line trip at 1 sec. sc=35% with DC-link voltage control. (10a): PLL 1. (10b): PLL 2.

TABLE IV: PFs of modes $\lambda_{6,7}$, $\lambda_{8,9}$ and $\lambda_{10,11}$ in Model 2

Description	**State Variable**	**DC-link voltage control**					
		PLL1(sc=20%)			PLL2(sc=35%)		
		$\lambda_{6,7}$	$\lambda_{8,9}$	$\boldsymbol{\lambda_{11,12}}$	$\lambda_{6,7}$	$\boldsymbol{\lambda_{8,9}}$	$\lambda_{11,12}$
DC-link	V_{dc}^2	0.0026	0.1268	**0.3445**	0.0043	0.0148	**0.4713**
Grid	$i_{1,d}^g$	0.0056	0.0752	0.0014	0.0106	0.0286	0.0034
	$i_{1,q}^g$	0.0041	0.0512	0.0026	0.0066	0.0461	0.0019
	$i_{g,d}^g$	0.0204	0.1375	0.0093	0.0361	0.0604	0.0143
	$i_{g,q}^g$	0.0289	**0.4308**	0.0061	0.0623	**0.2875**	0.0009
	$v_{PCC,d}^g$	0.0515	0.0615	0.0006	0.0985	0.00293	0.0002
	$v_{PCC,q}^g$	0.0199	0.0254	0.0016	0.0231	0.0229	0.0002
	$v_{c,d}^g$	**0.4224**	0.0899	0.0012	**0.3428**	0.1242	0.0005
	$v_{c,q}^g$	**0.4591**	0.0302	0.0020	**0.4331**	0.0344	0.0052
PLL	$\Delta\theta$	0.0021	**0.9587**	0.1089	0.0113	**0.5515**	0.0139
	$\Delta\omega$	0.0001	**0.3438**	0.0869	0.0021	**0.2693**	0.0137
Outer-loop	i_{1d}^c	0.0001	0.1399	**0.3392**	0.0010	0.0090	**0.4692**
	i_{1q}^c	0.0008	0.1325	0.1109	0.0015	0.0376	0.0361
Inner-loop	u_d	0.0002	0.0014	0.0017	0.0001	0.0005	0.0024
	u_q	0.0001	0.00594	0.0237	0.0002	0.0196	0.0031

The eigenvalue loci in Fig. 9 and Table III identified two high-frequency mode above 100 Hz ($\lambda_{1,2}$ and $\lambda_{4,5}$), and three oscillation modes below 100 Hz ($\lambda_{6,7}$, $\lambda_{8,9}$, and $\lambda_{11,12}$) which are significantly influenced by the varying compensation level.

The high-frequency modes above 100 Hz are associated with the shunt capacitor and grid inductor dynamics. Mode $\lambda_{6,7}$ with a frequency range 50 $\sim$ 100 Hz is associated with the

TABLE III: Modes description for the V_{dc} control under marginal conditions

	Modes	Eigenvalue	Damping ratio	Freq. (Hz)	Most relevant states
	$\lambda_{1,2}$	$-497.5 \pm 1906.4i$	0.253	303.4	C_F, L_g
	λ_3	-1197.5	-	-	-
	$\lambda_{4,5}$	$-93.9 \pm 868.7i$	0.107	138.3	C_F, L_g
PLL 1	$\lambda_{6,7}$	$-3.3 \pm 384.6i$	0.009	61.2	C_g
(sc=20%)	$\lambda_{8,9}$	$-35.6 \pm 63.9i$	0.487	10.2	PLL, L_g
	λ_{10}	-60.6	-	-	-
	$\boldsymbol{\lambda_{11,12}}$	$\mathbf{0.02 \pm 17.6i}$	**0.001**	**2.8**	$\boldsymbol{V_{dc}}$ **dynamic, Outer loop PI**
	λ_{13}	-11.4	-	-	-
	λ_{14}	-7.1	-	-	-
	λ_{15}	-6.9	-	-	-
	$\lambda_{1,2}$	$-550.3 \pm 1914.2i$	0.276	304.7	C_F, L_g
	λ_3	-1199	-	-	-
	$\lambda_{4,5}$	$-102.4 \pm 898.3i$	0.113	143.0	C_F, L_g
	$\lambda_{6,7}$	$-5.3 \pm 394.1i$	0.013	62.7	C_g
PLL 2	$\boldsymbol{\lambda_{8,9}}$	$\mathbf{0.0098 \pm 131.1i}$	**0.00007**	**20.9**	**PLL,** $\boldsymbol{L_g}$
(sc=35%)	λ_{10}	-91.3	-	-	-
	$\lambda_{11,12}$	$-1.5 \pm 19.9i$	0.075	3.2	V_{dc} dynamic, Outer loop PI
	λ_{13}	-11.1	-	-	-
	λ_{14}	-6.9	-	-	-
	λ_{15}	-6.9	-	-	-

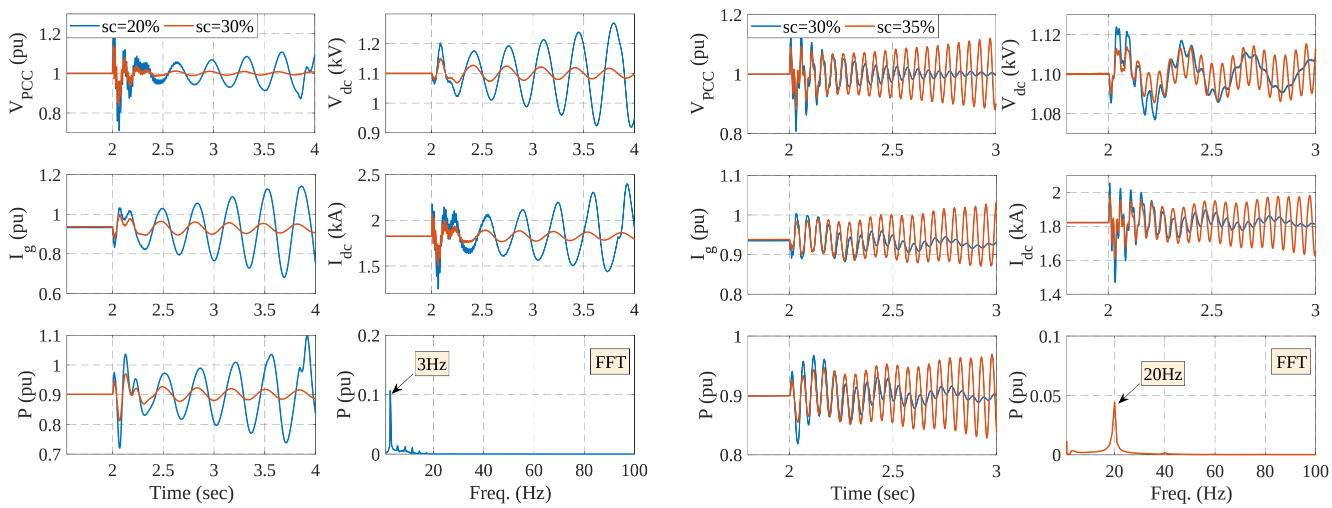

(a) (b)

Fig. 11: Dynamic performances of two compensation level under V_{dc} control in MATLAB/SimPowerSystems. (11a) PLL 1. (11b) PLL 2.

series capacitor. It moves to the LHP with increasing sc level. The $8 \sim 20$ Hz mode $\lambda_{8,9}$ is related to grid current and PLL. It moves towards the RHP with increasing series compensation level. The low-frequency ($2 \sim 5$ Hz) mode $\lambda_{11,12}$ is related to dc-link capacitor dynamics, outer control loop. It moves towards the LHP with increasing series compensation level.

When PLL 1 is applied, the low-frequency mode is the dominant mode. When PLL 2 is applied, the $8 \sim 20$ Hz mode is the dominant mode. Further more, increasing sc level poses stability risk for the case with PLL 2. In another word, PLL with high bandwidth may pose oscillatory stability issue for type-4 wind in series compensated network.

Time-domain simulation results based on Model 2 are presented in Fig. 10. The parallel RL circuit is tripped at $t = 1$ s, which leaves the type-4 wind radially connected to the series compensated line (sc is 35%). Simulation results show that the system is stable for PLL 1. However, for PLL 2, the system is unstable.

B. *EMT Testbed Validation*

The EMT dynamic validation results based on Testbed 2 are shown in Fig. 11. At the $t = 2$ s, the non-compensated line is tripped. 3 Hz oscillations are observed for the system with PLL 1. Increasing the sc level from 20% to 30% makes the system stable. On the other hand, a 20 Hz oscillations occur if PLL 2 is used. Increasing sc level from 30% to 35% makes the system unstable.

The dynamic performances corroborate with the results based on eigenvalue analysis shown in Fig. 9. That is, with the increasing compensation level, the low-frequency mode moves to the left and the $8 \sim 20$ Hz mode moves to the right. PLL has a great influence on the $8 \sim 20$ Hz mode and system stability. High PLL bandwidth leads to a dominant 20 Hz mode.

V. Impedance-based Stability Analysis

In the literature, frequency-domain impedance models are either measured using harmonic injection method (e.g., [25]) or derived by conducting linearization at every stage for every equation (e.g., [26], [27]). Alternatively, small-signal time-domain state space model is first derived, with linearization conducted at every stage for every equation. With a device's terminal voltage treated as the input and the current flowing into the device as the output, the admittance of the device may be found as the frequency-domain transfer function. This approach has been adopted in [7], [28]–[30] to find admittance or impedance models.

In this paper, a computing efficient approach of finding impedance through nonlinear analytical model is presented. Compared to the approach in the literature, linearization is carried out in one step via numerical perturbation.

Approach for obtaining the admittances of wind farm from the analytical model is illustrated in Fig. 12. The admittance of the wind farm viewed from the PCC bus is desired. To find the admittance, the integration system is constructed to have the PCC bus directly connected to the grid voltage source. Based on this assumption, the analytical model of the system is constructed in the dq-frame. Using numerical perturbation (e.g., Matlab command `linmod`), lineraized model can be found. An input/output linearized model is found with the dq-axis voltages as input and the dq-axis currents as output. This input/output representation is indeed the admittance model of the wind farm.

The linear model is a 2×2 admittance matrix as follows.

$$\begin{bmatrix} i_{s,d}(s) \\ i_{s,q}(s) \end{bmatrix} = \underbrace{\begin{bmatrix} Y_{dd}(s) & Y_{dq}(s) \\ Y_{qd}(s) & Y_{qq}(s) \end{bmatrix}}_{Y_{\mathrm{vsc},dq}} \begin{bmatrix} v_{s,d}(s) \\ v_{s,q}(s) \end{bmatrix} \tag{1}$$

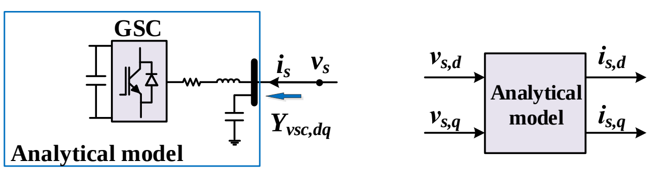

Fig. 12: Approach to find impedance/admittance.

For a series compensated transmission line, the impedance model in dq-domain is expressed as [31]:

$$Z_{L,dq} = \begin{bmatrix} R + Ls + \frac{s}{C(s^2+\omega_0^2)} & -L\omega_0 + \frac{\omega_0}{C(s^2+\omega_0^2)} \\ L\omega_0 - \frac{\omega_0}{C(s^2+\omega_0^2)} & R + Ls + \frac{s}{C(s^2+\omega_0^2)} \end{bmatrix} \tag{2}$$

A. System Stability Analysis

Impedance-based stability analysis is carried out for analytical model 2 (wind farm GSC in dc-link voltage control mode). Stability of a multi-input multi-output (MIMO) system can be assessed by the Generalized Nyquist Criterion (GNC), which has been popularly used in stability analysis, e.g., [32]–[35]. The loop gain of the system is defined in (3). The system will be unstable when characteristic loci of two eigenvalues of the loop gain (λ_1 and λ_2) encircle the point (-1, 0) clockwise in the Nyquist diagram. Instability is also reflected in Bode plots as the magnitude greater than 0 dB when the phase shift happens for the two eigenvalues.

$$L = Y_{\mathrm{vsc},dq} \times Z_{L,dq} \tag{3}$$

Fig. 13 presents a stable case (case 1: $sc = 25\%$) and an unstable case (case 2: $sc = 40\%$) for Model 2 with a high bandwidth PLL considered (PLL 2). For case 1, Fig. 13a Bode plot shows that phase shifting occurs at 22.58 Hz. The magnitude of the eigenvalue at 22.58 Hz is less than 1. Hence the system is stable. The Nyquist diagram in Fig. 13b indicates the contour does not encircle (-1,0). Hence the system is stable. For case 2, the Bode plot in Fig. 13c shows that phase shifting occurs at 21.5 Hz. The corresponding magnitude of the eigenvalue is greater than 1. Hence the system is unstable. Instability is also confirmed by the Nyquist diagram in Fig. 13d where (-1,0) is encircled clockwise.

The analysis results confirm the analysis in Section IV and the major finding of this paper: when series compensation is used to reduce electric distance for type-4 wind farm integration systems, instability may occur.

VI. Conclusion

In this paper, small-signal stability analysis of type-4 wind in series compensated network is conducted relying on state-space analytical models and impedance models. Under weak grid conditions, increasing series compensation level may pose oscillatory stability issues due to interaction of a weak grid mode and the LC resonance mode. Type-4 wind's GSC control parameters play a big role on the dominant mode and stability. The analysis presented in this paper is based on two analytical models built in dq-frames with grid dynamics and GSC control included. Analytical results and remarks are verified in two EMT testbeds with full dynamics, including grid dynamics, wind turbine mechanical and machine dynamics, and all stages of converter controls.

References

[1] J. Adams, C. Carter, and S.-H. Huang, "Ercot experience with sub-synchronous control interaction and proposed remediation," in *Transmission and Distribution Conference and Exposition (T&D), 2012 IEEE PES*. IEEE, 2012, pp. 1–5.

[2] S. Huang and Y. Gong, "South Texas SSR," http://www.ercot.com/content/wcm/key_documents_lists/139265/10._South_Texas_SSR_ERCOT_ROS_May_2018_rev1.pdf, May 2018.

[3] X. Xie, X. Zhang, H. Liu, H. Liu, Y. Li, and C. Zhang, "Characteristic analysis of subsynchronous resonance in practical wind farms connected to series-compensated transmissions," *IEEE Transactions on Energy Conversion*, vol. 32, no. 3, pp. 1117–1126, 2017.

[4] H. Ma, P. Brogan, K. Jensen, and R. Nelson, "Sub-synchronous control interaction studies between full-converter wind turbines and series-compensated ac transmission lines," in *Power and Energy Society General Meeting, 2012 IEEE*. IEEE, 2012, pp. 1–5.

[5] M. B. Beza and M. Bongiorno, "On the risk for subsynchronous control interaction in type 4 based wind farms," *IEEE Transactions on Sustainable Energy*, 2018.

[6] S.-H. Huang, J. Schmall, J. Conto, J. Adams, Y. Zhang, and C. Carter, "Voltage control challenges on weak grids with high penetration of wind generation: Ercot experience," in *Power and Energy Society General Meeting, 2012 IEEE*. IEEE, 2012, pp. 1–7.

[7] H. Liu, X. Xie, J. He, T. Xu, Z. Yu, C. Wang, and C. Zhang, "Subsynchronous interaction between direct-drive pmsg based wind farms and weak ac networks," *IEEE Transactions on Power Systems*, vol. 32, no. 6, pp. 4708–4720, 2017.

[8] N. P. Strachan and D. Jovcic, "Stability of a variable-speed permanent magnet wind generator with weak ac grids," *IEEE Transactions on Power Delivery*, vol. 25, no. 4, pp. 2779–2788, 2010.

[9] Y. Zhou, D. Nguyen, P. Kjaer, and S. Saylors, "Connecting wind power plant with weak grid-challenges and solutions," in *Power and Energy Society General Meeting (PES), 2013 IEEE*. IEEE, 2013, pp. 1–7.

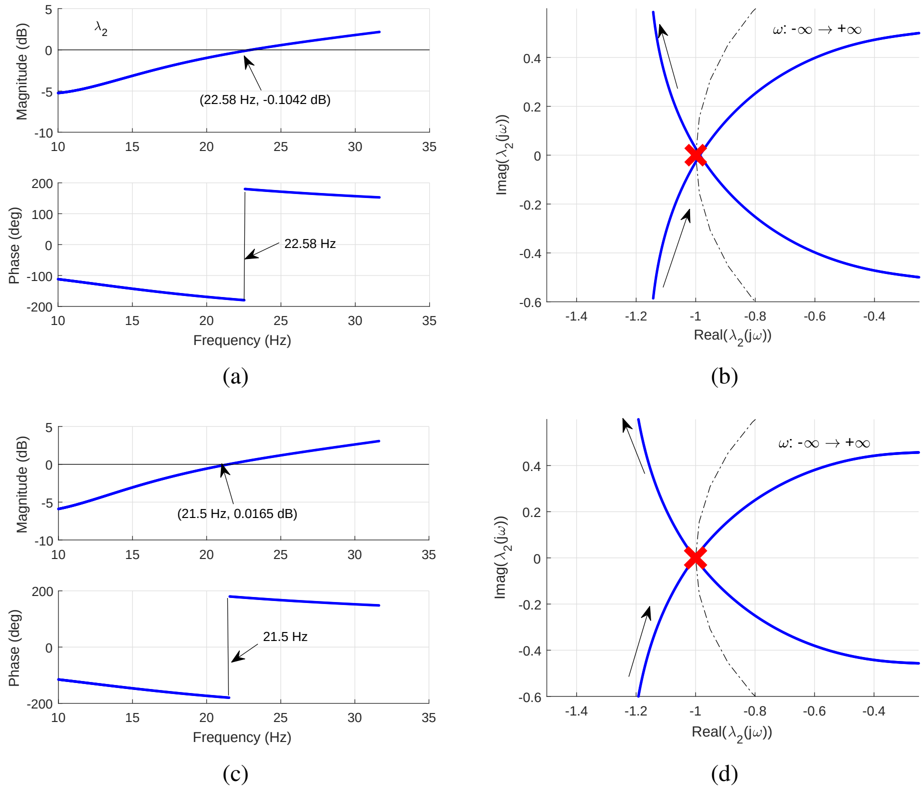

Fig. 13: Impedance-based stability analysis for Analytical model 2 with high bandwidth PLL applied. Upper row (13a)(13b): a stable case when compensation level is 25%. Lower row (13c)(13d): an unstable case when compensation level is 40%.

APPENDIX

TABLE V: Parameters of type-4 wind testbeds and analytical Models. (Values in pu if not specified)

Description		**Parameters**	**Values**
Testbed 1 PSCAD	base	Sb	5 MW
	Vbase	AC side	690 V, 33 kV
	Vbase	DC side	1500 V
	Power	P	1
	Line	X_g	1
	DC-link	C_{dc}	0.1 F
Testbed 2 MATLAB/ SimPower	base	Sb	100 MW
	Vbase	AC side	575 V, 25 kV, 220 kV
	Vbase	DC side	1100 V
	Power	P	0.9
	Line	X_g	0.7
	dc-link	C_{dc}	0.09 F
	dc/dc inductance	L_{boost}	1.2 mH
Poles		p	2
Rotor speed of generator		ω_r	1
Rated wind speed		v_w	11 m/s
Nominal frequency		f	60 Hz
Converter filter		R_F	0.003
		X_F	0.15
Shunt capacitor susceptance		B_c	0.3
Transformer T_1		R_{T1}	0.0005
		X_{T1}	0.005
Transformer T_2		R_{T2}	0.0005
		X_{T2}	0.005
X over R ratio		X/R	10
Inner current control		(K_{pi}, K_{ii})	0.4758, 3.2655
Power control		(K_{pp}, K_{ip})	0.25, 25
dc-link control		(K_{pp}, K_{ip})	0.25, 25
AC voltage control		(K_{pv}, K_{iv})	0.2, 20
PLL1		$(K_{p,pll1}, K_{i,pll1})$	60, 1400
PLL2 for Model 1, Testbed 1		$(K_{p,pll2}, K_{i,pll2})$	150, 10000
PLL2 for Model 2, Testbed 2		$(K_{p,pll2}, K_{i,pll2})$	150, 11000

[10] J. Hu, Y. Huang, D. Wang, H. Yuan, and X. Yuan, “Modeling of grid-connected dfig-based wind turbines for dc-link voltage stability analysis,” *IEEE Transactions on Sustainable Energy*, vol. 6, no. 4, pp. 1325–1336, 2015.

[11] M. Zhao, X. Yuan, J. Hu, and Y. Yan, “Voltage dynamics of current control time-scale in a vsc-connected weak grid,” *IEEE Transactions on Power Systems*, vol. 31, no. 4, pp. 2925–2937, 2016.

[12] J. Z. Zhou, H. Ding, S. Fan, Y. Zhang, and A. M. Gole, “Impact of short-circuit ratio and phase-locked-loop parameters on the small-signal behavior of a vsc-hvdc converter,” *IEEE Transactions on Power Delivery*, vol. 29, no. 5, pp. 2287–2296, 2014.

[13] H. Yuan, X. Yuan, and J. Hu, “Modeling of grid-connected vscs for power system small-signal stability analysis in dc-link voltage control timescale,” *IEEE Transactions on Power Systems*, 2017.

[14] L. Fan, “Modeling type-4 wind in weak grids,” *IEEE Transactions on Sustainable Energy*, vol. 10, no. 2, pp. 853–864, April 2019.

[15] L. Fan and Z. Miao, “Wind in weak grids: 4 hz or 30 hz oscillations?” *IEEE Transactions on Power Systems*, vol. 33, no. 5, pp. 5803–5804, Sep. 2018.

[16] L. Fan and Z. Miao, “An explanation of oscillations due to wind power plants weak grid interconnection,” *IEEE Transactions on Sustainable Energy*, vol. 9, no. 1, pp. 488–490, 2018.

[17] B. Wu, Y. Lang, N. Zargari, and S. Kouro, *Power conversion and control of wind energy systems*. John Wiley & Sons, 2011, vol. 76.

[18] X. Yuan, F. Wang, D. Boroyevich, Y. Li, and R. Burgos, “Dc-link voltage control of a full power converter for wind generator operating in weak-grid systems,” *IEEE Transactions on Power Electronics*, vol. 24, no. 9, pp. 2178–2192, Sept 2009.

[19] L. Fan, R. Kavasseri, Z. L. Miao, and C. Zhu, “Modeling of dfig-based wind farms for ssr analysis,” *IEEE Transactions on Power Delivery*, vol. 25, no. 4, pp. 2073–2082, 2010.

[20] Z. Miao, “Impedance-model-based ssr analysis for type 3 wind generator and series-compensated network,” *IEEE Transactions on Energy Conversion*, vol. 27, no. 4, pp. 984–991, 2012.

[21] J. Sun, Z. Bing, and K. J. Karimi, “Input impedance modeling of multipulse rectifiers by harmonic linearization,” *IEEE Transactions on Power Electronics*, vol. 24, no. 12, pp. 2812–2820, 2009.

[22] J. Sun, "Impedance-based stability criterion for grid-connected inverters," *IEEE Transactions on Power Electronics*, vol. 26, no. 11, p. 3075, 2011.

[23] M. Cespedes and J. Sun, "Impedance modeling and analysis of grid-connected voltage-source converters," *IEEE Transactions on Power Electronics*, vol. 29, no. 3, pp. 1254–1261, 2014.

[24] (2018, Dec) Type-4 Wind Turbine Model. [Online]. Available: https://hvdc.ca/uploads/knowledge_base/type_4_wind_turbine_model_v46.pdf?t=1544110359

[25] B. Badrzadeh, M. Sahni, Y. Zhou, D. Muthumuni, and A. Gole, "General methodology for analysis of sub-synchronous interaction in wind power plants," *IEEE Transactions on Power Systems*, vol. 28, no. 2, pp. 1858–1869, 2012.

[26] L. Harnefors, M. Bongiorno, and S. Lundberg, "Input-admittance calculation and shaping for controlled voltage-source converters," *IEEE transactions on industrial electronics*, vol. 54, no. 6, pp. 3323–3334, 2007.

[27] X. Wang, L. Harnefors, and F. Blaabjerg, "Unified impedance model of grid-connected voltage-source converters," *IEEE Transactions on Power Electronics*, vol. 33, no. 2, pp. 1775–1787, 2017.

[28] K. M. Alawasa, Y. A. I. Mohamed, and W. Xu, "Modeling, analysis, and suppression of the impact of full-scale wind-power converters on subsynchronous damping," *IEEE Systems Journal*, vol. 7, no. 4, pp. 700–712, Dec 2013.

[29] K. M. Alawasa, Y. A.-R. I. Mohamed, and W. Xu, "Active mitigation of subsynchronous interactions between pwm voltage-source converters and power networks," *IEEE Transactions on Power Electronics*, vol. 29, no. 1, pp. 121–134, 2013.

[30] H. Liu and X. Xie, "Comparative studies on the impedance models of vsc-based renewable generators for ssi stability analysis," *IEEE Transactions on Energy Conversion*, vol. 34, no. 3, pp. 1442–1453, Sep. 2019.

[31] L. Piyasinghe, Z. Miao, J. Khazaei, and L. Fan, "Impedance model-based ssr analysis for tcsc compensated type-3 wind energy delivery systems," *IEEE Transactions on Sustainable Energy*, vol. 6, no. 1, pp. 179–187, 2014.

[32] A. Rygg, M. Molinas, C. Zhang, and X. Cai, "A modified sequence-domain impedance definition and its equivalence to the dq-domain impedance definition for the stability analysis of ac power electronic systems," *IEEE Journal of Emerging and Selected Topics in Power Electronics*, vol. 4, no. 4, pp. 1383–1396, 2016.

[33] C. Desoer and Y.-T. Wang, "On the generalized nyquist stability criterion," *IEEE Transactions on Automatic Control*, vol. 25, no. 2, pp. 187–196, 1980.

[34] A. Nakhmani, M. Lichtsinder, and E. Zeheb, "Generalized nyquist criterion and generalized bode diagram for analysis and synthesis of uncertain control systems," in *2006 IEEE 24th Convention of Electrical & Electronics Engineers in Israel*. IEEE, 2006, pp. 250–254.

[35] D. Lumbreras Magallón, R. Barrios, A. Urtasun Erburu, A. Ursúa Rubio, L. Marroyo Palomo, P. Sanchís Gúrpide *et al.*, "On the stability of advanced power electronic converters: the generalized bode criterion," *IEEE Transactions on Power Electronics, vol. 34, no. 9, September 2019*, 2019.

Yangkun Xu (S'15) received the B.S. degree in electrical engineering Shandong University of Science & Technology (Qingdao, China) in 2012 and M.S. degree in electrical engineering from Florida Institute of Technology (Melbourne, Florida). He joined the University of South Florida Smart Grid Power Systems Lab in Jan. 2015 for Ph.D. study. His research interests include wind energy grid integration EMT modeling and impedance-based analysis.

Miao Zhang (S'15) received the B.S. degree in electrical engineering Hebei University of Architecture in 2012 and M.S. degree in electrical engineering from the University of South Florida (Tampa FL) in Dec 2017. He joined the University of South Florida Smart Grid Power Systems Lab in Jan, 2017 for Ph.D. study. His research interests include wind energy grid integration EMT modeling, power systems optimization, system identification, and data analysis.

Lingling Fan (SM'08) received the B.S. and M.S. degrees in electrical engineering from Southeast University, Nanjing, China, in 1994 and 1997, respectively, and the Ph.D. degree in electrical engineering from West Virginia University, Morgantown, in 2001. Currently, she is an Associate Professor with the University of South Florida, Tampa, where she has been since 2009. She was a Senior Engineer in the Transmission Asset Management Department, Midwest ISO, St. Paul, MN, form 2001 to 2007, and an Assistant Professor with North Dakota State University, Fargo, from 2007 to 2009. Her research interests include power systems and power electronics. Dr. Fan serves as an editor for IEEE Trans. Sustainable Energy and IEEE Trans. Energy Conversion.

Zhixin Miao (SM'09) received the B.S.E.E. degree from the Huazhong University of Science and Technology,Wuhan, China, in 1992, the M.S.E.E. degree from the Graduate School, Nanjing Automation Research Institute (Nanjing, China) in 1997, and the Ph.D. degree in electrical engineering from West Virginia University, Morgantown, in 2002.

Currently, he is with the University of South Florida (USF), Tampa. Prior to joining USF in 2009, he was with the Transmission Asset Management Department with Midwest ISO, St. Paul, MN, from 2002 to 2009. His research interests include power system stability, microgrid, and renewable energy.